SAND2020-1067J

Helium Diffusion in Tungsten Nanotendrils

M. A. Cusentino[1] and B. D. Wirth[2,3]

[1] Center for Computing Research, Sandia National Laboratories, Albuquerque, NM, USA

[2] Department of Nuclear Engineering, University of Tenneessee, Knoxville, TN, USA

[3] Fusion Energy Division, Oak Ridge National Laboratory, Oak Ridge, TN, USA

E-mail: mcusent@sandia.gov

June 2019

Abstract. We describe molecular dynamics simulations of helium implantation in geometries resembling tungsten nanotendrils observed in helium plasma exposure experiments. Helium atoms self-cluster and nucleate bubbles within the tendril-like geometries. However, helium retention in these geometries is lower than planar surfaces due to higher surface area to volume ratio which allows for continual bubble expansion and non-destructive release of helium atoms from the nanotendril. Limited diffusion of helium atoms deeper into the tendril was observed, and diffusion was enhanced with pre-existing, subsurface helium bubbles. Diffusion coefficients on the order of $10^{-12} - 10^{-11}\ m^2 s^{-1}$ were calculated. This suggests that while helium diffusion is low, it is still feasible that helium can diffuse to the base of a nanotendril to continue to drive fuzz growth.

1. Introduction

One of the main difficulties identified in engineering a viable fusion reactor is developing materials that can handle the harsh environment. Plasma facing components are subject to high temperatures, high ion fluxes of mixed particles, and high heat fluxes, especially at the divertor which will be subject to the most extreme loading conditions. Ion fluxes on the order of $10^{24}\ m^{-2}s^{-1}$ and heat loads on the order of 10 MW/m^2 are expected at the divertor in the International Thermonuclear Experimental Reactor (ITER) [1], and higher heat and particle fluxes are expected for subsequent fusion reactor generations. Currently, tungsten has been selected for the ITER divertor due to its high melting temperature, good thermal conductivity, and low sputtering yield [2]. While hydrogen isotopes are the majority of the ions striking the divertor, helium will be present in the plasma and has been shown to modify the tungsten microstructure in a variety of ways [1] [3]. Bubbles [4], pits [4], holes [5] [6], and fuzz [7] are just a few of the phenomena observed experimentally when tungsten is subject to high flux, low energy helium implantation at elevated temperatures. Tungsten fuzz is of major concern due to possible erosion of the observed nanotendrils and subsequent transport

to and contamination of the core plasma [8] as well as detrimental effects to the material performance of tungsten [9] which can negatively affect plasma performance [10].

Tungsten fuzz has been observed experimentally both in linear plasma devices [4] [7] [11] and tokomak experiments [12]. Conditions for fuzz growth are temperatures between 1000 K and 2000 K [13], helium energies of at least 20 eV [13], and fluences of at least 10^{24} m^{-2} [14]. The fuzz layer can extend beyond 10's of microns into the material although an individual nanotendril is only about 10-50 nm in diameter [11]. While the exact mechanism for fuzz formation is unknown, it is likely initiated by the nucleation and evolution of near surface helium bubbles [15]. The low energy helium atoms impinging at the divertor surface will implant within the first few nanometers of the surface [16] [17]. Since helium is chemically inert, the implanted atoms will not dissolve within tungsten but will instead self cluster if unable to diffuse to a free surface and desorb [18]. Eventually these initially mobile clusters become large enough to displace a tungsten atom and become a nucleation site for high pressure helium bubbles growth through a process called trap mutation [19]. These near surface bubbles will continue to grow through dislocation loop punching [20] [19] which can roughen the tungsten surface and this surface modification and continual bubble growth is believed responsible for the initial stages of fuzz formation [15]. TEM images have shown that nanotendrils do contain helium bubbles [9].

Various theories attempting to link the formation of helium bubbles to fuzz growth have been documented, including a method of continued surface roughening and bubble growth [9], a viscoelastic model of flowing tungsten atoms caused by helium bubbles [21], and a model of diffusing tungsten adatoms created by helium damage [22]. More recently, Dasgupta and co-workers have described a model based on the effect of bi-axial compressive stress in the helium bubble layer, which drives the initial surface roughness based on curvature driven diffusion from the flux of self-interstitial adatoms resulting from trap mutation and loop punching [23]. One major question is how helium, which implants within the first few nanometers of the surface, can be responsible for the continued growth of fuzz that is microns in length. The mechanism by which helium is able to reach the base of the fuzz is still unknown. Previous experimental and modeling work has attempted to answer this question. Experimental observations of the dependence of fuzz growth on the square root of exposure time [11] as well as an incubation fluence [14] suggest that diffusion plays a role in how helium reaches the base of the fuzz. Another theory is that the porosity of the tungsten fuzz will allow helium to penetrate through the fuzz layer to reach the base. Experiments have shown that tendrils can reach up to 90% porosity [24] which would provide open space to allow helium to travel much further into the fuzz layer than the initial helium implantation depth would suggest. Molecular dynamics has been used to study the effect of porosity on helium implantation [25], and found that the helium implantation depth depended on the open channel volume (e.g. porosity) and that helium implantation depths of a few hundred nanometers could be reached. However these simulations did not take into account electronic stopping, which will significantly decrease the kinetic energy of the

helium ions.

In this work, we model tungsten fuzz-like structures to assess helium retention, diffusion, and bubble evolution within these nanotendrils in order to better understand the early stages of fuzz growth and possible mechanisms by which helium can reach the base of the tendrils. The simulation methods and parameters are described in section 2. The results for both small and large tendril-like geometries are detailed in section 3 and the results are discussed in section 4. Finally, a summary of this work is given in section 5.

2. Methods

To study the helium behavior in tungsten nanotendrils, two sets of simulations are performed. The first set of simulations consisted of small, cylindrical 6 nm long and 5 nm wide tendrils while the second set consisted of large, 100 nm long and 25 nm wide parallelpiped shaped tendrils initially seeded with helium bubbles. Experiments show that the nanotendrils are 10-50 nm in diameter [11]. While the geometry in our simulations is on the low end of this spectrum, this work is meant to investigate early stage tendril growth. The exact geometry at the short timescales accessible by MD are experimentally unknown but the observation of larger nanotendrils that have some orientation has been documented [26] and the geometries used in this work are comparable.

For the smaller tendrils, the higher computational efficiency allowed for six different temperatures and five different geometries to be modeled. This provided information on helium diffusion and bubble nucleation and growth for varying initial simulation conditions that are linked to helium fuzz formation. However, the implantation fluxes are about three orders of magnitude too high which can affect helium diffusion. The second set of simulation alleviates this problem, the larger surface area leads to a lower implantation flux but with an increased computational cost. In addition, the parallelpiped is initially seeded on one end with helium bubbles. TEM experiments show the presence of cavities within the tendril, assumed to contain helium [9] which we expect to affect the evolution and diffusion of helium within the tendril. The lower flux combined with the longer tendril geometry allows for a more realistic study of helium diffusion to better address the still open question of how helium reaches the base of the nanontendrils.

We performed the molecular dyanmics simulations using the Large-scale Atomic/Molecular Massively Parallel Simulator (LAMMPS) [27] code. For tungsten, we used a Finnis-Sinclair potential [28] as modified by Ackland and Thetford [29] and further modified by Juslin and Wirth [30]. For W-He, a pair potential developed by Juslin and Wirth [30] was used. For the He-He interactions, a pair potential developed by Beck [31] and further modified by Morishita et al. [32] for short range interactions was used.

We performed similar helium implantations for both sets of simulations. The initial

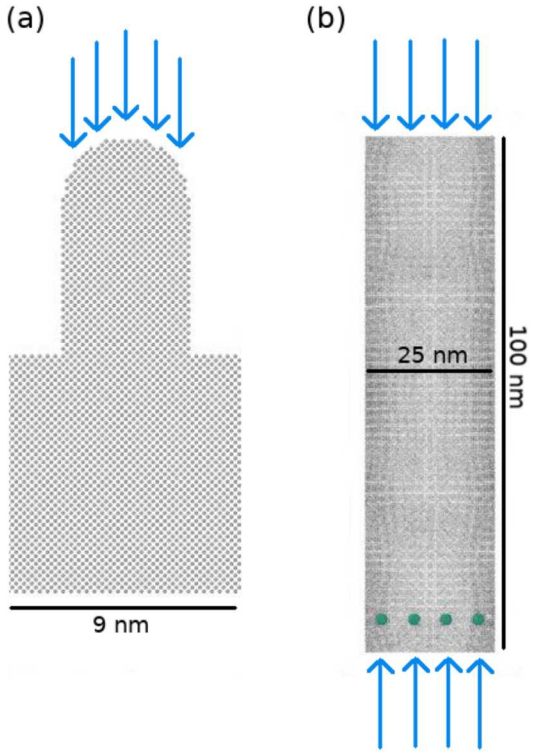

Figure 1: Initial configuration for the (a) small tendril and (b) large parallelpiped. The grey and green atoms represent the tungsten atoms and helium atoms in the pre-existing bubbles, respectively. The blue arrows indicate where helium is implanting into the tendril.

geometry for the small tendrils and large parallelpipeds are shown in Fig. 1 (a) and (b), respectively. For the small tendrils (Fig. 1(a)), a 9 nm x 9 nm x 9 nm tungsten block with periodic boundaries in the x and y directions and a (100) free surface in the z direction was first created. A tungsten cylinder 6 nm in height and 5 nm in diameter was centered on top of the block. Finally, a half sphere 5 nm in diameter was placed on top of the cylinder to complete the tungsten nanotendril geometry. For the large parallelpipeds (Fig. 1(b)), the geometry was modified by first removing the bulk region that was included in the small tendrils since we are most interested in diffusion down the tendril. The tendril shape was a parallelpiped as opposed to a cylinder with dimensions of 25 nm x 25 nm x 100 nm. At one end of the tendril, twelve bubbles with a 1 nm radius and helium concentration of 3 He/Vacancy were placed around the edge of the parallelpiped at a depth of 6 nm. The parallelpiped had free surfaces in all three directions and both (100) and (111) surface orientations were modeled. In both cases, the tungsten was then equilibrated to the appropriate temperature by first selecting velocities from a Maxwell-Boltzmann distribution. Velocity rescaling was the performed every 100 timesteps for 5 ps with an NVE thermostat followed by 15 ps with no velocity rescaling for 15 ps. A timestep of 1 fs was used during equilibration.

After equilibration, helium implantation dynamics were performed. The helium

was implanted every 10 ps using the 60 eV depth profile calculated in SRIM [33], and inserted at thermal energies based on the approach described by Sefta et al [19]. This leads to a flux of $1.2 \cdot 10^{27} m^{-2} s^{-1}$ and $1.6 \cdot 10^{26} m^{-2} s^{-1}$ for the small and large tendrils respectively. For the small tendrils, the helium was implanted strictly in the tendril, accounting for the curvature of the top of the tendril. For the large parallelpiped, helium was implanted on both ends of the parallelpiped to study the effects of pre-existing helium bubbles on the diffusion of implanted helium atoms. The blue arrows in Fig. 1 denote the region of helium implantation A total of 20,000 helium atoms were implanted in all cases, corresponding to a fluence of $2.4 \cdot 10^{20} m^{-2}$ and $3.2 \cdot 10^{19} m^{-2}$ for the tendril and parallelpiped, respectively. In both cases, it was necessary to fix tungsten atoms to prevent drift during the simulation. The bottom three layers of atoms were fixed for the small tendrils while the center of mass of each face was fixed for the parallelpipeds. Multiple temperatures were used for the small tendrils. The different temperatures included 1200 K, 1500 K, 1700 K, 1800 K, 1900 K, and 2000 K which are all within the expected temperature range for fuzz formation. In contrast, the parallelpiped simulations were held at 1200 K, near the temperature threshold for nanotendril formation. The timestep used depended on the temperature. Between 1200 K and 1700 K, the timestep was 0.5 fs, while at 1800 K and above, the timestep was 0.1 fs. At higher temperatures, the helium is more mobile and therefore a smaller timestep was needed in order to conserve energy. We also varied the geometry of the small tendril while keeping the temperature at 1200 K. The height was both increased to 8 nm and decreased to 4.8 nm from the base case of 6 nm. Radii of 1.3 nm and 3.8 nm were also compared with the base case of 2.5 nm. This leads to a total of 10 different temperature and geometry combinations for the small tendrils. In contrast, only two parallelpiped simulations with differing surface orientations of (100) and (111) were performed due to the higher computational cost.

3. Results

3.1. Small Tendril Results

After implantation into the tendril, the helium self clusters and forms bubbles that are comparable to previous MD simulations of planar tungsten surfaces [19] [16]. Figure 2 depicts atomistic snapshots at a fluence of $2.4 \cdot 10^{20}$ m^{-2} for temperatures of 1200 K, 1500 K, and 2000 K. A distribution of helium bubbles can be seen for all three cases that are strictly within the tendril. Helium self-trapping, which is more pronounced at higher implantation fluxes, prevents the helium from diffusing much past the implantation depth which means the bubbles will also remain near the top of the tendril. Although there are fairly large sized bubbles present within the tendril, there is very little deformation of the tendril surface itself. Some roughening exists, which is due to dislocation loop punching from bubble expansion, but the tendril more or less retains the initial shape. In fact, the tendril remains stable throughout the simulations even

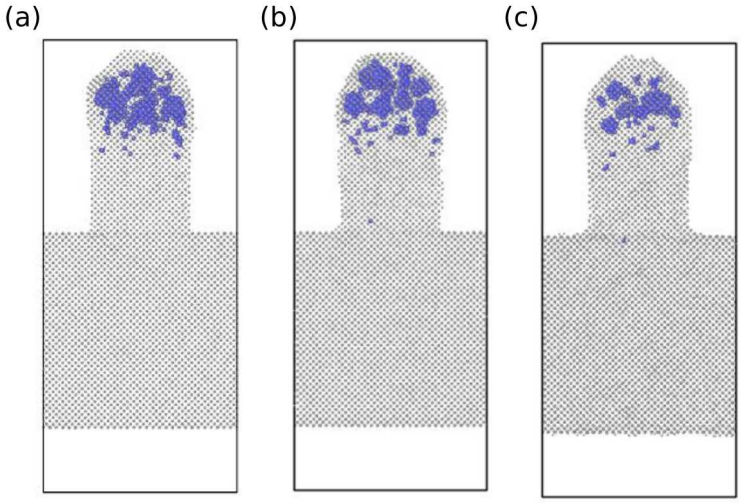

Figure 2: Atomistic snapshots of the small tendrils at 200 ns and a fluence of $2.4 \cdot 10^{20}$ m^{-2} for temperatures of (a) 1200 K, (b) 1500 K, and (c) 2000 K. Grey and blue atoms represent tungsten and helium respectively.

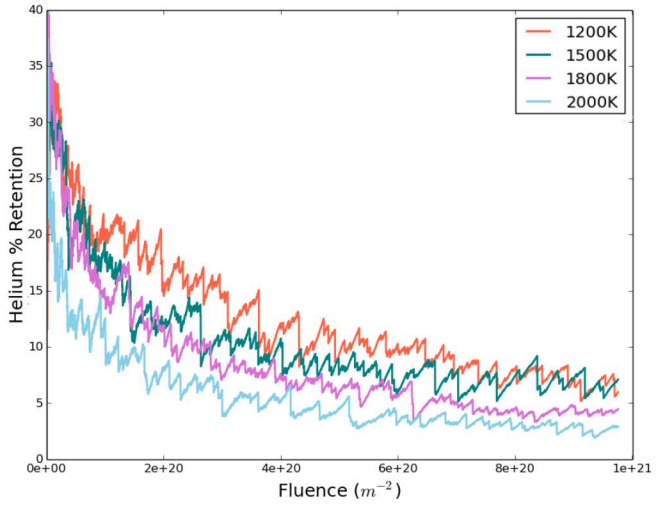

Figure 3: Helium retention (%) as a function of implanted helium fluence for nanotendrils at 1200 K (orange), 1500 K (teal), 1800 K (pink), and 2000 K (blue).

at 2000 K which is near the upper temperature threshold of tendril formation observed in experiments [13]. At 2000 K there is less total helium retained, as well as smaller bubbles but this could partially be dependent at the point in time at which the the snapshot was viewed.

The helium retention as a function of fluence is shown in Figure 3 for select temperatures. Each line depicts a single simulation over the entire 20 ns but is representative of other independent simulations at the same temperature. The retention is initially very high but quickly decreases to values under 20%. At increasing fluences,

the retention profile flattens out to an approximate steady state value of around 10% or lower. This is in contrast to previous MD simulations of planar surfaces which show a much higher retention of about 60% for simulations with a similar flux on the order of 10^{27} $m^{-2}s^{-1}$ and 40% for fluxes of 10^{25} $m^{-2}s^{-1}$ [34]. A higher retention would be expected at the high fluxes used here but this is not observed. The retention becomes very jagged even after trending towards a steady state. This indicates that as helium is added into the tendril, the retention increases until the bubbles become overpressurized to the point that the bubble bursting mechanism occurs, leading to rapid release of helium and thus a decrease in retention. This process repeats itself until the retention reaches a point that as helium is added to the tendril, roughly the same amount will be released leading to the steady state nature of the retention at higher fluences.

The helium retention in a tendril-like geometry is quite different from that in a planar surface geometry. For a planar surface, the helium accumulates just below a tungsten surface leading to pressurized bubbles that can cause loop punching, adatom formation, or even bursting events with destructive surface deformation like cratering. In the tendril-like geometry case, helium bubbles will form similarly but the larger surface to volume ratio of the tendril will allow the bubbles to release helium much more easily without destructive bubble bursting events. In addition, the smaller available volume within the tendril limits the maximum size of bubble growth. The combination of larger surface area and lower available volume is responsible for the continual bubble growth and helium release without any significant surface deformation. Rather than destructive bubble bursting events, a modified helium release mechanism was observed, in which small pinhole ruptures are created from expanding bubbles. The pinhole ruptures correspond to the drops in retention in Figure 3. After many of the helium atoms escape the bubble, the pinhole self-heals and the remaining cavity can continue to accumulate helium.

The approximately steady-state helium retention decreases as a function of temperature. The average percent retention at 1200 K, 1500 K, 1700 K, and 2000 K was 6.8%, 6%, 4%, and 3.3% respectively. In addition, there are larger bubbles at lower temperatures (Figure 2). We further quantified the size of the largest bubbles as well as the total number of bubbles in the tendril. This analysis was performed for the last 20 ns of the simulation during the 'steady state' retention phase using a cutoff of 0.3 nm to determine if a helium atom identified within in a bubble. The distribution of bubbles was calculated every 10 ps and the largest bubble as well as total number of bubbles at each time interval was recorded. Over the 20 ns, the size of the largest bubble before releasing helium was noted. The average largest bubble size and total number of bubbles is shown in Table 1. The standard deviation was calculated using the averages across five simulations at each temperature. The average size of the largest bubble remains between 100 and 250 atoms for all temperatures. The average size at the lowest temperature of 1200 K is slightly larger, about 225 helium atoms, while at moderate temperatures between 1500 K and 1800 K, the values are fairly consistent at about 175 helium atoms. At 2000 K, the average largest bubble is only 110 helium

Table 1: Average Helium Bubble Properties as a Function of Temperature

Temperature	Largest Bubble	Total Number of Bubbles	He/V Ratio
1200	225 ± 70	65 ± 8	1.8 ± 1.5
1500	170 ± 50	58 ± 5	1.5 ± 1.0
1700	216 ± 40	52 ± 6	1.3 ± 0.7
1800	165 ± 80	47 ± 6	1.2 ± 0.9
2000	114 ± 42	30 ± 3	1.1 ± 0.6

atoms. While it is important to note that the variability between runs is quite large, it is clear that the helium bubbles are smaller at 2000 K than at 1200 K which is consistent with visual observations. The trend in average number of clusters within the tendril is even more evident. Again, at lower temperatures the average total number of bubbles is around 65 at 1200 K but only 30 at 2000 K. These values also tend to be more consistent at the different temperatures, having smaller error bars on the order of 5 bubbles. The combination of larger, more numerous bubbles in the lower temperature simulations explains the higher retention.

The helium bubbles grow and expand through dislocation loop punching. This has been observed in previous simulations involving planar surfaces with typical helium concentrations of 3-4 He/V that correspond to gas pressures well above equilibrium [35] for bubbles a few nanometers below the surface. The helium concentration for bubbles within the tendril were also calculated, using a Wigner-Seitz defect analysis and cluster analysis in OVITO [36] and are reported in Table 1. The Wigner-Seitz analysis is used to determine where the vacancies and interstitial helium atoms are located. A cluster analysis is then used to calculate how many helium atoms and vacancies are clustered together. Error bars are again calculated across the five simulations performed at each temperature. On average, the ratio is between 1 He/V and 2 He/V, which is comparable for bubbles below planar surfaces for the same ligament thickness as the bubbles in the tendril simulations [35]. In contrast, bubbles further below a planar surface at 4 nm have a higher He/V value of 3-4. However, the error bars at each temperature are fairly large. For example at 1200 K, the He/V ranged from 0.5 to 8 He/V. For the largest bubbles, the He/V ratio tended to be between 1.3 and 2.1 with lower temperatures having a slightly higher value. The lower He/V ratio within the bubbles indicates that these are lower pressure bubbles than would be seen in a simulation with a planar surface. This observation can be explained by the larger surface area to volume ratio, which allows for easier release of helium and, correspondingly lower helium concentrations and pressures within the bubbles themselves. The lower helium concentrations observed in the bubbles within tendrils at increasing temperature also indicates that the pin hole rupture phenomena occurs more readily at higher temperatures.

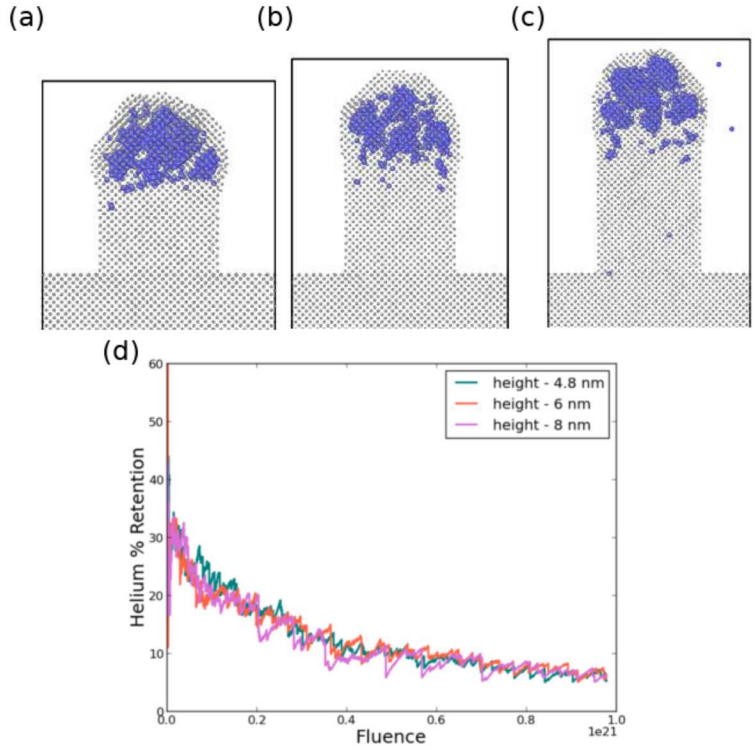

Figure 4: Atomistic snapshots of helium implantation in nanotendrils of varying height (a) 4.8 nm, (b) 6 nm, and (c) 8 nm where grey and blue are the tungsten and helium atoms respectively. A plot of helium percent retention as a function of fluence is shown in (d) where green, orange, and pink depict 4.8, 6, and 8 nm respectively.

3.2. Variation on Small Tendril Geometry

The initial study involved helium implantation in a fixed nanotendril geometry as a function of temperature. The next varied parameter was the tendril height and radius. We further investigated the evolution of tendril-like structures for heights of 4.8 and 8.0 nm compared with the nominal height of 6.4 nm, as well as radii of 1.3 nm and 3.8 nm compared to the nominal case of 2.5 nm. All of these MD simulations were performed at 1200 K using the same helium flux. Figure 4 depicts atomistic snapshots of the helium bubble populations with variation in the tendril height. Helium retention and bubble distributions for varying height nanotendrils are comparable to simulations with the initial geometry. Most of the retained helium remains near the top of the tendril and has not diffused deeper into the tungsten despite the change in tendril dimension. For all three heights, the helium percent retention decreases and reaches an approximately steady-state value of about 7% at the end of the simulation. The distribution and depth of the helium bubbles is also comparable for all three heights.

On the other hand, varying the radii at a constant helium implantation rate did affect the overall helium inventory in the tendril, as indicated in Figure 5, again for simulations at 1200 K. For a radius of 1.3 nm (Fig. 5(a)), there is very little helium

observed within the tendril and only one large bubble was present even at a fluence of 10^{21} m^{-2}. In contrast, the tendril with an increased 3.8 nm radius (Fig. 5(c)) had a much higher concentration of helium with a wider distribution of varying bubble sizes residing within the tendril. These observations are consistent with the helium retention, which is plotted in Figure 5(d) as a function of fluence. At the end of the 200 ns simulation, the overall percent retention for the 1.3 nm, 2.5 nm, and 3.8 nm radius tendrils are about 4%, 7%, and 13%, respectively. However, the helium is implanted at a constant rate, which due to the different radii of the tendril, results in a different flux and fluence. Due to the large surface area of the 3.8 radius tendril and constant rate of helium implantation, the fluence only reaches a value of $4 \cdot 10^{20}$ m^{-2}. An inset image is included to highlight the fluences where data from all three simulations is available. In the inset image, the helium retention for the 2.5 nm and 3.8 nm tendrils are comparable, with retention values of around 12%, due to the shorter simulation time for the 2.5 nm tendril at that particular fluence. Therefore, while the height does not seem to affect the retention or tendril evolution, the radius does. This can also be explained by the different surface to volume ratio. For a cylinder, the surface area is defined as $2\pi RH$ and the volume is defined as $\pi R^2 H$ where R and H are the radius and height respectively. Therefore, the ratio is proportional to $1/R$. In the case of varying the height, the surface to volume ratio remains the same since the radius is kept consistent. However, when varying the radius this ratio does in fact change due to the $1/R$ relationship. Therefore, the volume increases more than the surface area with increasing radius which can result in more helium self-clustering reactions and more retained helium in the larger radius tendrils.

For most simulations, the helium remained near the implantation depth at the top of the tendril due to self-trapping. The high flux used in these simulations allows for helium bubbles to form quickly and does not allow enough time for helium to diffuse deeper into the tendril. However, in a few cases, a helium atom or two managed to diffuse down to the bottom of the tendril. This is an interesting observation since these helium atoms are outliers in the cumulative depth distribution. One of the open questions related to fuzz formation is the mechanism by which helium reaches the bottom of nanotendrils. For cases discussed in relation to Figure 2, simulations at higher temperatures are more likely to have helium atoms diffuse to the base of the tendril. However, these are limited observations with insufficient statistics and the helium atoms may or may not diffuse to the base of the tendril between simulations even with the same conditions. An additional way to perturb the system to see the impact on helium diffusion is to include an initial distribution of helium bubbles within the tendril to evaluate how the presence of pre-existing helium bubbles affects helium diffusion. It is possible that the stress in the matrix from pre-existing helium bubbles could bias diffusion toward the pre-existing bubbles and therefore modify the final helium depth distribution. Therefore a set of large-scale simulations with pre-existing helium bubbles were performed to both assess the effect of lowered helium flux and pre-existing helium bubbles on helium diffusion in tendril-like geometries.

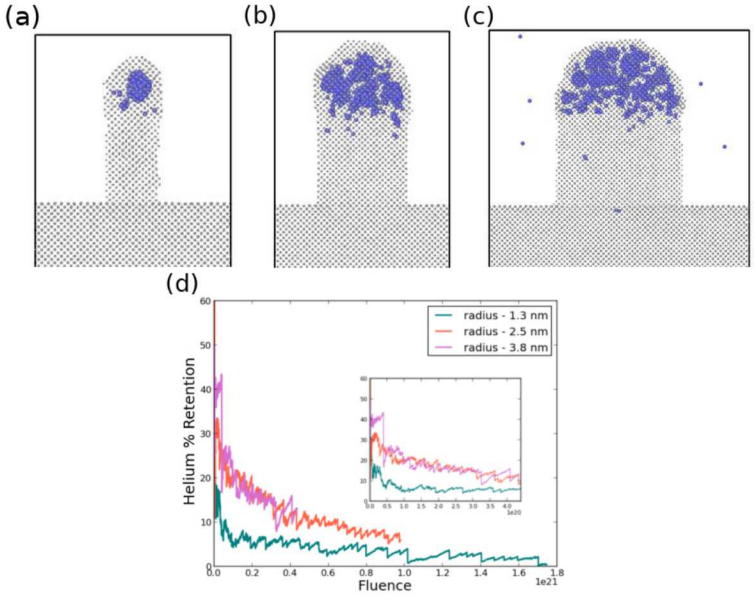

Figure 5: Atomistic snapshots of helium implantation in small tendrils of radii (a) 1.3 nm, (b) 2.5 nm, and (c) 3.8 nm where grey and blue are the tungsten and helium atoms respectively. A plot of helium percent retention as a function of fluence for the entire simulation is shown in (d) where green, orange, and pink depict 1.3, 2.5, and 3.8 nm respectively. The inset image depicts helium retention for the three cases but only up to a fluence of $4 \cdot 10^{20} m^{-2} s^{-1}$

3.3. Large-scale Tendril Results

The large-scale parallelpiped geometries used a helium implantation flux of $1.6 \cdot 10^{26} m^{-2} s^{-2}$ in which helium was inserted from both ends of the parallelpiped geometry at 1200K to a fluence of $3.2 \cdot 10^{19}\ m^{-2}$, a total of 200 ns of simulation time. Figure 6 depicts atomistic snapshots of the parallelpiped geometries at the end of the simulation for the (a) (100) and (b) (111) surface without pre-existing bubbles and the (c) (100) and (d) (111) surface with pre-existing bubbles. The blue and green atoms represent implanted helium and helium initially in pre-existing bubbles respectively. A large portion of helium atoms exist within the first two nanometers of the surface. This is expected due to the self-trapping of helium atoms especially once a population of helium bubbles has nucleated. In fact, the helium retention is quite high for all four cases, 88% and 83% for the (100) surface with and without pre-existing bubbles and 72% and 82% for the (111) surface with and without pre-existing bubbles, respectively. The surface to volume ratio is lower for the large parallelpiped cases which leads to higher magnitudes of helium retention than for the small tendril geometries described previously. In addition, the fluence is about two orders of magnitude lower for the large parallelpiped case. The effect of the pre-existing helium bubbles on retention is small for the (100) surface, for which only a 5% increase is observed. In contrast, the retention is 10% lower with pre-existing helium bubbles below the (111) surface (relative to no

pre-existing bubbles).

Some limited diffusion of helium atoms deeper into the material occurs and tends to be slightly more pronounced for the (111) surface and for the cases with pre-existing helium bubbles. The depth distribution for all four cases was quantified and plotted in Figure 7. The green and orange lines represent the (100) and (111) surface while the solid and dotted lines represent the cases with and without pre-existing helium bubbles. In all cases, the helium diffuses to a depth of 6 nm. While this is deeper than observed for the small tendril cases, it is only a fraction of the 100 nm length of the parallelpiped. In neither simulation has a helium atom diffused from one end of the parallelpiped to the other. For both surface orientations, the helium atoms implanted near pre-existing bubbles diffuse deeper than for the case without pre-existing bubbles as indicated by the shifted depth profiles shown in Figure 7 by the solid lines. This is consistent with observations made by visualizing the atomistic snapshots. The pre-existing bubbles create stress within the tungsten which can assist the diffusion of helium by introducing a drift force that biases diffusion deeper into the material. This effect competes with helium self-trapping and is likely to be more effective at lower fluences before a large population of helium bubbles nucleate just below the surface. This can be seen by comparing the small and larger tendril cases. Virtually no atoms diffused past the initial implantation depth for the small tendrils which can be attributed to the high flux which leads to rapid helium bubble formation, in addition to the lower overall retention. These helium bubbles form quickly enough that they block the diffusion of other helium atoms which instead are absorbed by the growing bubbles. In contrast, at the lower fluence of the large parallelpiped simulations, more time for the helium to diffuse into the material before the near surface region becomes saturated with helium bubbles. However, even in the parallelpiped case, the amount of helium diffusing deep into the material decreases over time as the competing effects of trap mutation begin to dominate. For example, in the (100) case the percent of implanted atoms that diffuse past 5 nm is 0.05%, 0.18%, 0.27%, and 0.46% for 5 ns, 10 ns, 15 ns, and 20 ns, respectively. Initially, the number of diffusing helium atoms triples bewteen 5 and 15 ns but eventually the rate of diffusion declines later in the simulation. By 10 ns, a network of sub-surface helium bubbles has been established which prevents further helium diffusion into the material. For the small tendril case, even at 2000 K only 1 atom has diffused to the base of the tendril, accounting for only 0.005% of the implanted helium. The high flux, and therefore more rapid initiation of trap mutation, further limits helium diffusion and demonstrates the strength of trapping at helium bubbles. On the other hand, if there are indeed helium bubbles that form deeper in an actual nanotendril, it could provide a driving force for additional helium atoms to diffuse further down the nanotendril.

The presence of pre-existing helium bubbles affects the helium concentration profile and allows for a higher amount of helium to be present deeper in the material. The helium concentration as a function of depth is plotted in Figure 8. The cases with pre-existing bubbles are shown in (a) and (b) for the (100) and (111) surface, respectively, while the cases without pre-existing bubbles are shown in (c) and (d) for the (100) and

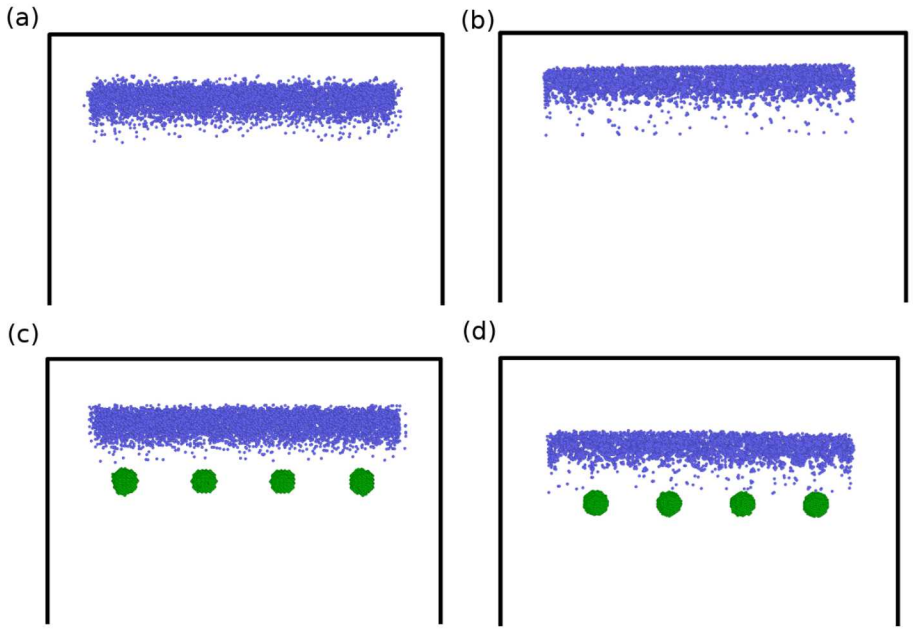

Figure 6: Atomistic snapshots of the parallelpiped geometry at a fluence of $3.2 \cdot 10^{19} m^{-2}$ for the (a) (100) and (b) (111) surface without pre-existing helium bubbles and the (c) (100) and (d) (111) surface with pre-existing helium bubbles. The blue and green atoms represent implanted helium and helium initially in a pre-exsiting bubble respectively. Tungsten atoms are not shown.

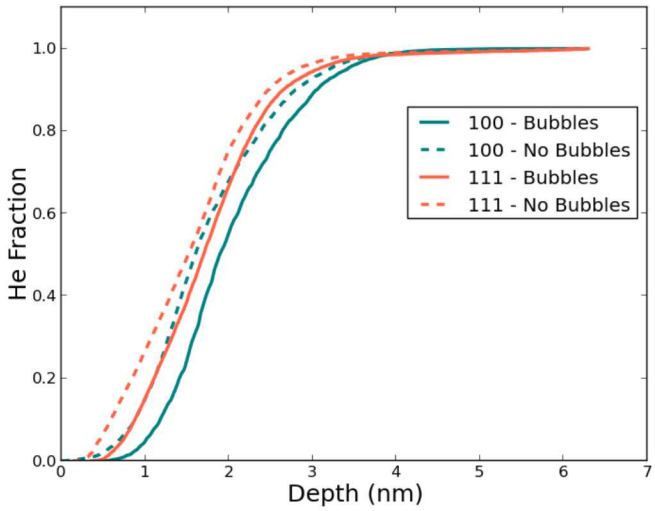

Figure 7: Plot of the normalized helium depth distribution at a fluence of $3.2 \cdot 10^{19} m^{-2}$. The orange and green represent the (100) and (111) surfaces and the solid and dotted lines represent the case with and without pre-existing helium bubbles respectively.

(111) surface, respectively. The blue, pink, green, and orange lines are the concentration profiles at 5 ns, 10 ns, 15 ns, and 20 ns, respectively. The concentration profiles follow a

similar trend with a peak in helium concentration at 2 nm below the surface that drops off fairly quickly out to 6 nm. The peaks are higher for the (100) surface due to the higher retention compared to the (111) surface. While the peaks in helium concentration are located at 2 nm for all cases, the profiles are skewed towards the surface for the cases without pre-existing bubbles and towards the pre-existing helium bubbles for the cases with them. This is clearly shown for both the (100) and (111) surface. At 20 ns, the (100) surface with pre-existing bubbles has a concentration of about $5 \cdot 10^{27}$ He/m^3 at 3 nm while the case without pre-existing bubbles has a slightly lower concentration of $4 \cdot 10^{27}$ He/m^3 at 3 nm. The contrast is even stronger for the (111) surface which has a concentration of $3.5 \cdot 10^{27}$ He/m^3 at 3 nm for the case with pre-existing helium bubbles at 3 nm but less than $2 \cdot 10^{27} He/m^3$ at 3 nm for the case without pre-existing bubbles at 20 ns. The helium concentrations also tend to be about twice as large at 1 nm for the cases without pre-existing helium bubbles, again demonstrating a bias for helium to diffuse deeper into the material when pre-existing bubbles are present.

The change in helium concentration over time appears to depend on both the depth and the presence of pre-existing helium bubbles. While the increase in helium concentration over time at 2 nm or below appears to increase over time, the opposite is true for larger depths. The increase in concentration at 4 nm, for example, from 5 ns to 10 ns is larger than from 10 to 15 ns and so on. The increasing concentration over time at 2 nm is due to the helium continually being implanted near this depth and the increased self-trapping over time as helium bubble nuclei continue to form. At larger depths, the helium is initially able to diffuse further into the material while the population of helium bubble nuclei near the surface is low. However, over time the amount of near-surface helium bubbles increases which leads to a greater likelihood that newly implanted helium becomes trapped at these bubbles instead of diffusing further into the parallelpiped. This trend is even more apparent for cases without pre-existing helium bubbles. For example, for the (111) surface without pre-existing bubbles the helium concentration at 4 nm remains very close to zero for nearly the entire simulation (Figure 8d). In contrast, the (111) case with pre-existing bubbles has a measureable helium concentration at 5 ns for a depth of 4 nm although the concentration increase slows over time. Both the shape of the helium concentration profile as well as the evolution with increasing time indicates that the pre-existing helium bubbles are affecting the diffusion of helium atoms within the parallelpiped.

3.4. Helium Diffusion Coefficient Calculations

The concentration profiles can be used to calculate an effective helium diffusion coefficient using a solution to the time dependent 1-D diffusion equation. While an exact, analytical solution to the diffusion equation using conditions present in these simulations is difficult, if not impossible to find, the closest analytical solution to the concentration data can be used as an approximation to solve for the diffusion coefficient. For this work, the analytical solution that assumes an initial release of particles into

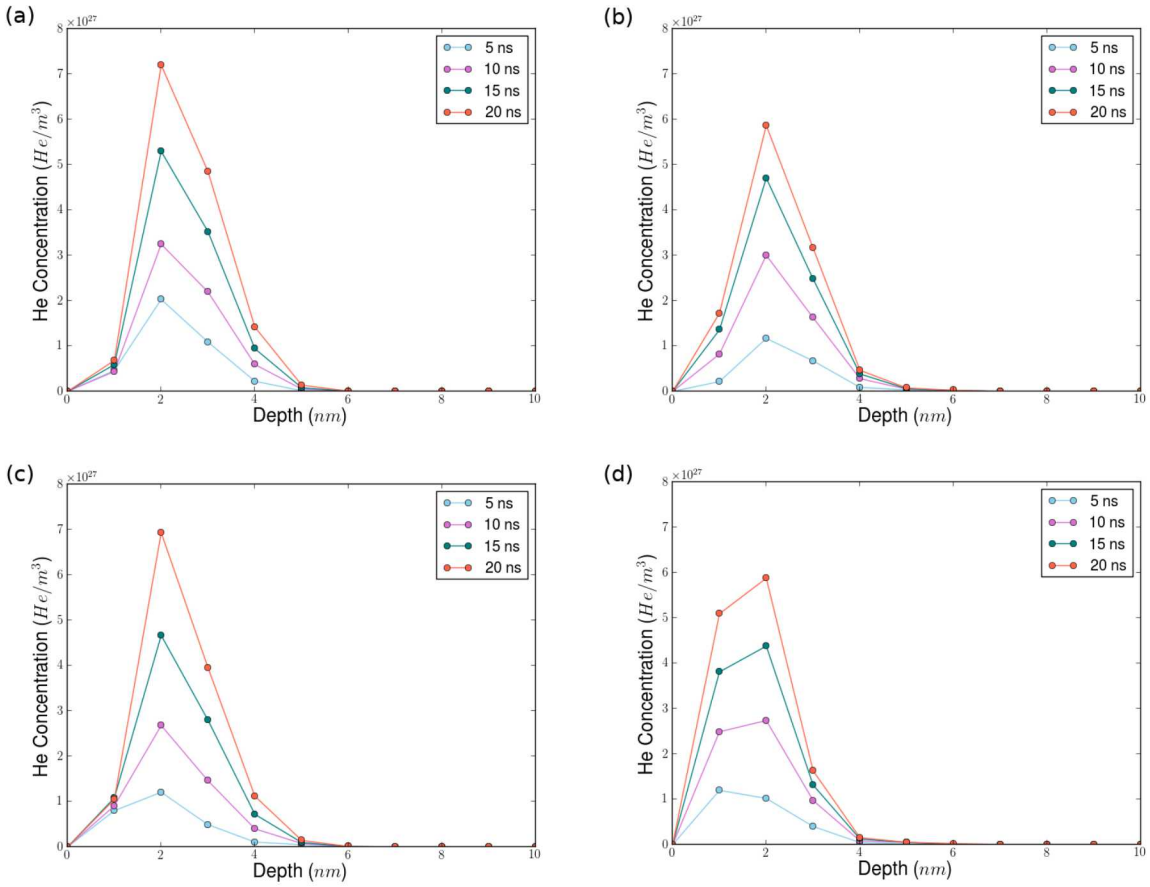

Figure 8: Plots of the helium concentration profiles as a function of depth for the (a) (100) and (b) (111) surfaces with pre-existing helium bubbles and the (c) (100) and (d) (111) surfaces without pre-existing helium bubbles. The blue, pink, green, and orange lines represent concentration profiles at 5 ns, 10 ns, 15 ns, and 20 ns respectively.

a pristine material is used. While in these simulations the helium is continually being thermally inserted into the material at various depths, the concentration profile from the peak to a depth of 6 nm mimics the shape of an analytical solution and the assumption that particles are released at a particular point is somewhat consistent with placing helium atoms at their implantation depth into the material. The analytical solution follows the form

$$c(x,t) = \frac{N}{\sqrt{4\pi Dt}} exp(-\frac{x^2}{4Dt}) \tag{1}$$

where $c(x,t)$ is the concentration at position x and time t, N is the number of particles initially released, and D is the diffusion coefficient. To calculate D, equation 1 was fit to the data in Figure 8 for each of the 4 cases at 5 ns, 10 ns, 15 ns, and 20 ns, respectively, and for depths between 2 nm, where many of the helium atoms were being implanted, and 6 nm, the furthest the helium atoms were diffusing. Since N represents the total number of particles initially released, this value was set to the total number of helium

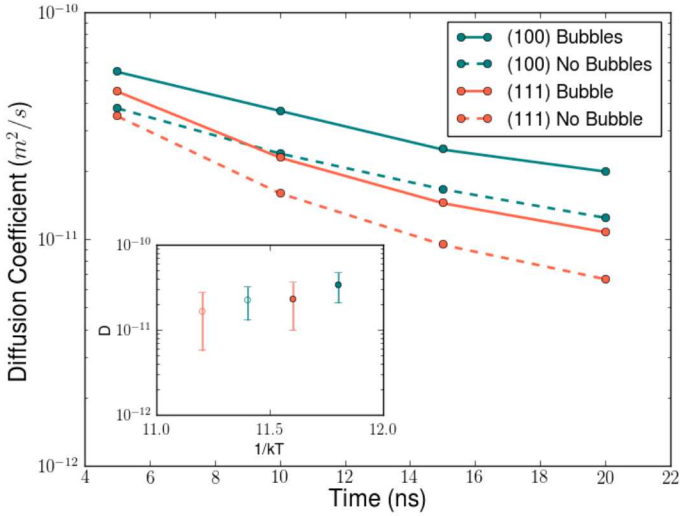

Figure 9: Plot of the diffusion coefficients as a function of time for the (100) surface (teal) and (111) surface (orange) with pre-existing bubbles (solid) and without pre-existing bubbles (dotted). The inset image represents an average diffusion coefficient for each case as a function of 1/kT where the filled circles and open circles represent the case with and without pre-existing bubbles respectively. Note that 1/kT for all cases is 11.6 but the markers are offset to better see the data.

atoms between 2 nm and 6 nm. The concentration, $c(x,t)$, was then set to the value at the x distance of 6 nm for each t value between 5 and 20 ns. D was then solved for using this criteria and a value for each time for all four cases was calculated.

The resulting diffusion coefficients are plotted as a function of time in Figure 9. The green and orange lines represent the (100) and (111) surface and the solid and dotted lines represent the case with and without pre-existing helium bubbles, respectively. The inset image depicts the average diffusion coefficient over the relatively short 20 ns time duration, with corresponding error bars as a function of 1/kT. The closed and open circles represent the case with and without pre-existing helium bubbles, respectively. Note that 1/kT is 11.6 for all 4 cases, since all simulations are held at 1000 K, but the points are offset to better depict the data. The diffusion coefficient ranges from approximately $6 \cdot 10^{-12}$ to $5 \cdot 10^{-11}$ m^2/s.

Using an activation energy of 0.15 eV for helium interstitial migration obtained from this interatomic potential [37], a jump frequency of 10^{13} 1/s, and a jump length of 1.117 $\mathring{A}$, a diffusion coefficient of $5 \cdot 10^{-9}$ m^2/s is calculated from the Arrhenius equation. This is significantly higher than the trap mediated diffusion coefficients calculated in this work. This implies that the presence of helium bubbles can affect helium diffusion by a factor of up to three orders of magnitude. Further, as noted in the concentration profiles, the diffusion coefficient decreases during the simulation by about a factor of 3 for the (100) surface and a factor of 5 for the (111) surface. This result can again be

ascribed to the increase of near surface helium bubbles over time that can trap the newly implanted helium atoms. The other impact of helium bubbles is shown in the difference between the simulations with and without pre-existing helium bubbles. After 20 ns, the diffusion coefficient for the pre-existing helium bubbles cases is both higher and has decreased less over the initial 20 nanoseconds of simulated time than the case without pre-existing helium bubbles. Despite initially having similar diffusion coefficients, the pre-existing bubble simulations lead to helium diffusivity values that are a factor of 1.2 and 1.6 higher at 20 ns for the (100) and (111) surface, respectively. Again, the presence of deep helium bubbles seems to drive the helium atoms further into the tungsten matrix and slow the decrease in the diffusion coefficient over time.

4. Discussion

Both the small tendril and large parallelpiped simulations provide insight into the behavior of helium atoms in nanotendrils. One of the main results of these simulations is that the large amount of free surface available in tendril geometries reduces helium retention. The larger surface area per unit volume allows for helium to more readily escape from the tendril without any major surface deformation leading to an overall lower helium inventory compared to a planar surface. A planar surface has a higher confining stress compared to the tendril geometries, due to the lower available surface area, which leads the bubbles to overpressurize. Varying the tendril radii further demonstrated this behavior, a tendril with a smaller radius had even lower retention while a tendril with an larger radius had higher retention. The initial results from the smaller tendril-like geometry indicate that there exists a relationship between the helium retention and the surface to volume ratio of the tendril geometry. In the case of the large parallelpipeds, the retention was much higher than for the small tenderil simulations but the surface area to volume ratio was much lower. The parallelpipeds had a higher internal volume to hold helium with a limited amount of surface area which resulted in a higher helium retention. Combining the results of both sets of simulations, the helium retention is plotted as a function of surface area to volume ratio. A power law relation was obtained, as plotted in Figure 10 along with the simulation data. All data points calculated in this work are plotted as black circles and the corresponding trendline is indicated by the black line. The resulting fit to the data is:

$$f(x) = 16.791 \cdot x^{-0.504} \tag{2}$$

where f(x) is the retention and x is the surface area to volume ratio. Also plotted in Figure 10 are retention data for a (100) and (111) planar surface from Ref. [34] that are indicated by the green and orange squares, respectively. An estimated helium retention for a characteristic 50 nm diameter, 1 micron long tendril is denoted by the blue star in Figure 10. The retention was calculated using the power law relation, which predicts a helium retention of about 60%, although it is important to note that Eq. (2) does not incorporate any dependence on helium implantation flux which is known to significantly

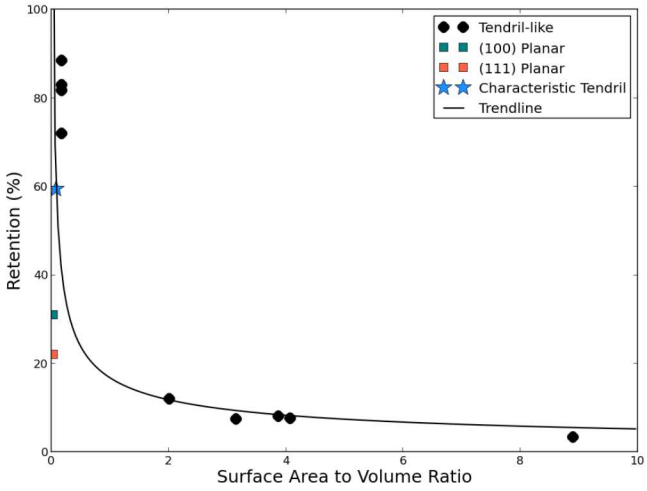

Figure 10: Plot of the helium retention as a function of surface area to volume ratio. The tendril-like geometry simulations presented in this work are plotted as black circles with a power law trendline while retention values for planar surfaces from [34] are plotted as squares for the (100) surface (green) and (111) surface (orange). The blue star represents an extrapolation of the data for a characteristic tendril observed in experiments that is 50 nm in diameter and 1 microns in length.

impact retention, at least for the realtively high fluxes accessible in atomistic MD simulations [34]. While the planar surfaces have a smaller surface to volume ratio than the large parallelpipeds, the helium retention is about half that compared to the parallelpiped simulations. This may be due to the relatively low fluences reached in the parallelpiped geometries in this work in addition to the higher implantation flux, although additional simulation time to a comparable fluence might lower the retention. The observed relationship between helium retention and surface area to volume ratio could provide a means to determine the expected helium retention for a given tendril geometry from experiments or other modeling work

One unanswered question is how helium reaches the base of the tungsten fuzz to continue to grow more nanotendrils into the material. The implantation depth of helium is on the order of a few nanometers while the fuzz can grow up to microns in length, which suggests that there might be some method for helium to reach the base of the fuzz. Other mechanisms, such as helium implantation through the fuzz layer to the base, have been proposed [25], our work suggests that helium diffusion may play a role. In this work, limited diffusion of helium past the near-surface helium bubble layer has been observed to depths of about 6 nm for the large parallepiped simulations. Concentrations profiles as a function of depth and time were used to estimate diffusion coefficients for diffusion in tendrils both with and without pre-existing helium bubbles. The diffusion coefficients varied between 10^{-12} to 10^{-11} $m^{-2}s^{-1}$ with lower values occuring at longer times and without pre-existing helium bubbles. Using these diffusion coefficients (Figure

9 and the geometry of a characteristic nanotendril from experiments), an estimation of the time it would take for a helium atom to diffuse to the base of a nanotendril can be obtained from the expression for one dimensional diffusion:

$$D = \frac{< x >^2}{2t} \tag{3}$$

where D is the diffusion coefficient, $< x >$ is the mean displacement, and t is the time it takes to travel $< x >$. Using a 1 micron, 10 micron, or 100 micron long tendril and an average diffusion coefficient of $2.43 \cdot 10^{-11}$ $m^2 s^{-1}$, the time for a helium atom to diffuse the entire length of the tendril would be 0.02 seconds, 2.1 seconds, and 205.8 seconds, respectively. This is within the time it takes to form fuzz, which is typically on the order of minutes to 10s of minutes. Therefore, the results of this work suggest that helium diffusion to the base of the tendril cannot be entirely ruled out. While helium was not observed to diffuse past 6 nm in the large parallelpiped simulations, the 20 ns of simulated time in these MD simulations is very short compared to the time that would be needed for helium to diffuse to more significant depths in the material. This is likely outside of the time attainable by MD so other methods would be needed to extrapolate the observations in this work. In addition, the characteristic diffusion time calculated here will likely be a lower bound estimate since it is unknown if the helium will avoid being absorbed by other bubbles. Nonetheless, this work indicates the possibility that helium diffusion may be responsible for helium atoms that reach the base of tungsten fuzz.

5. Conclusions

In this work, we have modeled helium implantation in a nanotendril-like geometry using molecular dynamics in order to study helium retention and diffusion in a geometry similar to experimentally observed tungsten fuzz. Helium bubble nucleation and growth is similar to that in planar surfaces. However, due to the larger surface area available to desorb helium, helium bubbles are allowed to continually grow, expand, and release helium atoms non-destructively within the tendril-like geometry. This allows for a steady state concentration of helium that is lower than observed for planar surfaces. We have noted a relationship between helium retention and surface to volume ratio, such that higher surface to volume ratios allow for helium to escape (desorb) much more easily and leads to lower helium retention, about 10% compared to 30-60% for planar surfaces. Our investigation of helium diffusion in tendrils lead to the conclusion that while diffusion is limited due to the rapid growth of near-surface helium bubbles that can trap implanted helium atoms, there is some limited diffusion deeper into the material. The presence of helium bubbles initially placed past the implantation depth can increase the helium diffusion deeper into the material. Diffusion coefficients on the order of $10^{-12} - 10^{-11}$ $m^2 s^{-1}$ were calculated for this trapping mediated behavior. Even though the diffusion coefficients were observed to decrease over time and helium was not observed past 6 nm within these 20 nanosecond MD simulations, the diffusion values calculated indicate the

potential for helium diffusion to the base of a 10 micron long nanotendril in about 200 seconds, consistent with the time it takes to form fuzz. Therefore, this study suggests that helium diffusion down nanotendrils cannot entirely be ruled out as a mechanism for transporting helium to the base of the tendrils to continue tungsten fuzz growth.

6. Acknowledgements

All authors gratefully acknowledge funding support is from the plasma surface interaction project of the Scientific Discovery through Advanced Computing (SciDAC) program, which is jointly sponsored by the Fusion Energy Sciences (FES) and the Advanced Scientific Computing Research (ASCR) programs within the U.S. Department of Energy Office of Science. This research used resources of the National Energy Research Scientific Computing Center (NERSC), a U.S. Department of Energy Office of Science User Facility operated under Contract No. DE-AC02-05CH11231. Sandia National Laboratories is a multi-mission laboratory managed and operated by National Technology and Engineering Solutions of Sandia, LLC, a wholly owned subsidiary of Honeywell International, Inc., for the U.S. Department of Energy's National Nuclear Security Administration under contract DE-NA0003525. This paper describes objective technical results and analysis. Any subjective views or opinions that might be expressed in the paper do not necessarily represent the views of the U.S. Department of Energy or the United States Government.

References

[1] G. Federici, C. Skinner, J. Brooks, J. Coad, C. Grisolia, A. Hassz, A. Hassanein, V. Philipps, C. Pitcher, J. Roth, W. Wampler, and D. Whyte. Plasma-material interactions in current tokamaks and their implications for the next step fusion reactors. *Nuclear Fusion*, 41:1967–2137, 2001.

[2] R.A. Pitts, S. Carpenter, F. Escourbiac, T. Hirai, V. Komarov, S. Lisgo, A.S. Kukushikin, A. Loarte, M. Merola, A.S. Naik, R. Mitteau, M. Sugihara, P. Bazylev, and P.C. Stangeby. A full tungsten divertor for iter: Physics issues and design status. *Journal of Nuclear Materials*, 438:S48–S56, 2013.

[3] K.D. Hammond. Helium, hydrogen, and fuzz in plasma-facing materials. *Materials Research Express*, 4:104002, 2017.

[4] H. Iwakiri, K. Yasunaga, K. Morishita, and N. Yoshida. Microstructure evolution in tungsten during low-energy helium ion irradiation. *Journal of Nuclear Materials*, 283-287:1134–1138, 2000.

[5] D. Nishijima, M.Y. Ye, N. Ohno, and S. Takamura. Formation mechanism of bubbles and holes on tungsten surface with low-energy and high-flux helium plasma irradiation in nagdis-ii. *Journal of Nuclear Materials*, 329-333:1029–1033, 2004.

[6] D. Nishijima, M. Miyamoto, H. Iwakiri, M. Ye, N. Ohno, K. Tokunaga, N. Yoshida, and S. Takamura. Micron-bubble formation on polycrystal tungsten due to low-energy and high-flux helium plasma exposure. *Materials Transactions*, 46:561–564, 2005.

[7] S. Takamura, N. Ohno, D. Nishijima, and S. Kajita. Formation of nanostructured tungsten with arborescent shape due to helium plasma irradiation. *Plasma and Fusion Research*, 1:051, 2006.

[8] K.R. Umstadter, R. Doerner, and G. Tynan. Effect of bulk temperature on erosion of tungsten

plasma-facing components subject to simultaneous deuterium plasma and heat pulses. *Physica Scripta*, 2009:014047, 2009.

[9] S. Kajita, S. Takamura, N. Ohno, D. Nishijima, H. Iwakiri, and N. Yoshida. Sub-ms laser pulse irradiation on tungsten target damaged by exposure to helium plasma. *Nuclear Fusion*, 47:1358–1366, 2007.

[10] K.W. Hill, M. Bitter, D. Eames, S. von Goeler, M. Goldman, N.R. Sauthoff, and E. Silver. Low energy x-ray emission from magnetic fusion plasmas. Technical Report PPPL-1807, Princeton, 01 1982.

[11] M.J. Baldwin and R.P. Doerner. Helium induced nanoscopic morphology on tungsten under fusion relevant plasma conditions. *Nuclear Fusion*, 48:038001, 2008.

[12] G.M. Wright, D. Brunner, M.J. Baldwin, K. Bystrov, R.P. Doerner, B. Labombard, G. Lipschultz, B.and De Temmerman, J.L. Terry, D.G. Whyte, and K.B. Woller. Comparison of tungsten nano-tendrils grwon in alcator c-mod and linear plasma devices. *Journal of Nuclear Materials*, 438:S84–S89, 2013.

[13] S. Kajita, W. Sakaguchi, N. Ohno, N. Yoshida, and T. Saeki. Formation process of tunsten nanostructure by the exposure to helium plasma under fusion relevant plasma conditions. *Nuclear Fusion*, 49:095005, 2009.

[14] T.J. Petty, M.J. Baldwin, M.I. Hasan, R.P. Doerner, and J.W. Bradley. Tungsten 'fuzz' growth re-examined: the dependence on ion fluence in non-erosive and erosive helium plasma. *Nuclear Fusion*, 55:09033, 2015.

[15] S. Kajita, N. Yoshida, R. Yoshihara, N. Ohno, and M. Yamagiwa. Tem obervation of the growth process of helium nanonbubbles on tungsten: Nanostructure formation mechanism. *Journal of Nuclear Materials*, 418:152–158, 2011.

[16] K.D. Hammond and B.D. Wirth. Crystal orientation effects on helium ion depth distributions and adatom formation processes in plasma-facing tungsten. *Journal of Applied Physics*, 116:143301, 2014.

[17] V. Borovikov, A.F. Voter, and X.-Z. Tang. Reflection and implantation of low energy hehlium with tungsten surfaces. *Journal of Nuclear Materials*, 447:254–270, 2014.

[18] X.-C. Li, Y.-N. Liu, G.-N. Luo, X. Shu, and G.-H. Lu. Helium defects interactions and mechanism of helium bubble growth in tungsten: A molecular dynamics simulation. *Journal of Nuclear Materials*, 451:356–360, 2014.

[19] F. Sefta, K.D. Hammond, N. Juslin, and B.D. Wirth. Tungsten surface evolution by helium bubble nucleation growth and rupture. *Nuclear Fusion*, 2013:073015, 2013.

[20] A.M. Ito, Y. Yoshimoto, S. Saito, A. Takayama, and H. Nakamura. Molecular dynamics simulation of a helium bubble bursting on tungsten surfaces. *Physica Scripta*, 2014:014062, 2014.

[21] S.I. Krasheninnikov. Viscoelastic model of tungsten 'fuzz' growth. *Physica Scripta*, T145:014040, 2011.

[22] Y.V Martynenko and M.Y. Nagel. Model of fuzz formation on a tungsten surface. *Plasma Physics Reports*, 38:996–999, 2012.

[23] D. Dasgupta, R.D. Kolasinski, R.W. Friddle, L. Du, D. Maroudas, and B.D. Wirth. On the origin of fuzz formation in plasma facing materials. *Nuclear Fusion*, 59:086057, 2019.

[24] M.J. Baldwin and R.P. Doerner. Formation of helium induced nanostructure fuzz on various tungsten grades. *Journal of Nuclear Materials*, 404:165–173, 2010.

[25] T.P.C. Klaver, K. Nordlund, T.W. Morgan, E. Westerhof, B.J. Thijsse, and M.C.M van de Sanden. Molecular dynamics simulations of ballistic he penetration into w fuzz. *Nuclear Fusion*, 56:126015, 2016.

[26] K. Wang, R.P. Doerner, M.J. Baldwin, F.W. Meyer, M.E. Bannister, A. Darbal, R. Stroud, and C.M. Parish. Morphologies of tungsten nanotendrils grown under helium exposure. *Scientific Reports*, 7:42315, 2017.

[27] S. Plimpton. Fast parallel algorithms for short-range molecular algorithms. *Journal of Computational Physics*, 117:1–19, 1995.

[28] M. Finnis and J. Sinclair. A simple empirical n-body potential for transition metals. *Philisophical Magazine A*, 50:45–55, 1984.

[29] G.J. Ackland and Thetford R. An improved n-body semi-empirical model for body-centered cubic transition metals. *Philisophical Magazine A*, 56:15–30, 1987.

[30] N. Juslin and B.D. Wirth. Interatomic potentials for simulation of he bubble formation in w. *Journal of Nuclear Materials*, 423:61–66, 2013.

[31] D. Beck. A new interatomic potential function for helium. *Molecular Physics*, 14:311–315, 1968.

[32] K. Morishita, R. Sugano, B.D. Wirth, and T.D. de la Rubia. Thermal stability of helium-vacancy clusters in iron. *Nuclear Instruments and Methods in Physics Research Section B*, 202:76–81, 2003.

[33] J.F. Ziegler, J.P. Biersack, and M.D. Ziegler. *The Stopping and Range of Ions in Solids*. Springer, Morrisville, 2008.

[34] B.D. Wirth, K.D. Hammond, S.I. Krasheninnikov, and D. Maroudas. Challenges and opportunities of modeling plasma-surface interactions in tungsten using high performance computing. *Journal of Nuclear Materials*, 463:30–38, 2015.

[35] K. Hammond, S. Blondel, L. Hu, D. Maroudas, and D. Wirth. Large-scale atomistic simulations of low-energy helium implantation into tungsten single crystals. *Acta Materiala*, 144:561–578, 2018.

[36] A. Stukowski. Visualization and analysis of atomistic simulation data with ovito - the open visualization tool. *Modelling and Simulation in Material Science and Engineering*, 18:015012, 2010.

[37] D. Perez, T. Vogel, and B.P. Uberuaga. Diffusion and transformation kinetics of small helium clusters in bulk tungsten. *Physical Review B*, 90:014102, 2014.